Influence of Spanwise Twisting and Bending on Lift Generation in MAV-Like Flapping Wings

Bruno A. Roccia[1]; Sergio Preidikman[2]; Marcos L. Verstraete[3]; and Dean T. Mook[4]

Abstract: A numerical-simulation tool is developed that is well suited for modeling the unsteady and nonlinear aerodynamics of flying insects and small birds as well as biologically inspired flapping-wing micro air vehicles (MAVs). The tool consists of a combination of (1) an aerodynamic model that is an extension of the widely used three-dimensional (3D) general unsteady vortex-lattice model, and (2) a general kinematic model that is capable of describing multiple deformation patterns of lifting surfaces, such as spanwise twisting, in-plane and out-of-plane bending, and any combination of these. Moreover, the present tool offers an attractive compromise between computational cost and fidelity and is ideally suited to be combined with computational structural dynamics to perform aeroelastic analyses. The present tool was successfully validated by comparing some of the present results with those obtained from existing numerical models based on both Euler equations and vortex-lattice codes and with some experimental data. Using the numerical framework developed and for the deformation mechanisms analyzed here, two distinctly different effects were found: the wing span's twisting and in-plane bending affect the lift in specific zones of the stroke cycle (called "local behavior"); and the wing span's out-of-plane bending affects the lift throughout the stroke cycle (called "global behavior"). In addition, the results found show that the wing's flexibility certainly affects the lift production, at least for some flights at small scales. These findings definitely suggest the strong likelihood that the unsteady vortex-lattice method combined with a general kinematic model can be a very accurate and efficient tool for future aeroelastic studies. **DOI: 10.1061/(ASCE)AS.1943-5525.0000677.**
© *2016 American Society of Civil Engineers.*

Downloaded from ascelibrary.org by Bruno Antonio Roccia on 08/05/16. Copyright ASCE. For personal use only; all rights reserved.

Introduction

In the early years, scientists and engineers used classical aerodynamic theories developed for conventional aircraft to try to understand how small insects and birds stay aloft. The application of these theories to the study of flight in nature (natural flight) led to a famous paradox: "a bee cannot fly" (McMasters 1989). In fact, conventional aerodynamic models yield very good results for steady flows over stationary bodies. However, natural flight is characterized by highly nonlinear and unsteady flows because of the complex combinations of the rigid and deforming motions of wings. Wing-deformation patterns include time-dependent bending, camber, spanwise twist, expansion and contraction of the lifting surfaces, and so forth.

Over the past four decades, researchers around the world have carried out several studies of the kinematics, aerodynamics, and flight dynamics of flying insects. Some important insights into the unsteady flow of flapping wings were obtained by assuming rigid-flat wings (Dickinson et al. 1999; Ellington et al. 1996; Liu et al. 1998; Wang et al. 2004), and works intended for characterizing the role of wing deformation on lift production, which is crucial to clearly understanding natural flight. Dalton (1975, 1982) published high-speed photographs of several free-flying insects, which showed wing deformations in various maneuvers. Weis-Fogh (1973) was the first to describe the unsteady aerodynamic mechanism in insect flight known as clap and fling. In the same article, he also proposed a series of additional mechanisms involving transient wing deformation. Norberg (1972), in what may have been the first experimental study of the structural mechanics of wings, highlighted the need of wings to adapt to resist aerodynamic twisting in flight. A few years later, Ellington (1984) described an analytical projection technique that allows one to study the angle of attack, camber, transverse bending, and twist of the wings of a marmalade hoverfly, a fruit fly, and a bumblebee. Subsequently, a variety of techniques have been developed to identify and quantify deformation patterns on different insect wings (Ennos 1989; Zeng et al. 1996; Song et al. 2001; Wang et al. 2003, 2009a, b, c, Aguayo et al. 2010; Lehmann et al. 2011; Mountcastle and Combes 2013).

More recently, and because of advances in computational and robotic technologies, two different approaches have been used to quantify the importance of wing flexibility on the aerodynamic forces of flapping wings. On the one hand, several numerical models were developed in order to study the fluid-structure interaction (either by using or by not using prescribed deformation patterns) on different flying insects; all of these predicted an increase in lift when the wing is allowed to deform (Ishilhara et al. 2009; Vanella et al. 2009; Young et al. 2009; Nakata and Liu 2012; Du and

[1]Associate Professor, Dept. of Structures, School of Exact, Physical, and Natural Sciences, Universidad Nacional de Córdoba, Av. Velez Sarsfield 299, 5000 Córdoba, Argentina; Assistant Investigator, Institute for Advanced Studies in Engineering and Technology, National Scientific and Technical Research Council IDIT-CONICET, Av. Velez Sarsfield 299, 5000 Córdoba, Argentina (corresponding author). E-mail: bruno.roccia@gmail.com

[2]Full Professor, Dept. of Structures, School of Exact, Physical, and Natural Sciences, Universidad Nacional de Córdoba, Av. Velez Sarsfield 299, 5000 Córdoba, Argentina; Independent Investigator, Institute for Advanced Studies in Engineering and Technology, National Scientific and Technical Research Council IDIT-CONICET, Av. Velez Sarsfield 299, 5000 Córdoba, Argentina.

[3]Postdoctoral Student, Dept. of Basic Sciences, Engineering School, Universidad Nacional de Río Cuarto, Ruta Nacional 36 km 601, 5800 Río Cuarto, Argentina.

[4]Waldo Harrison Professor Emeritus, Dept. of Biomedical Engineering and Mechanics, Virginia Polytechnic Institute and State Univ., Norris Hall, Room 333N, Virginia Tech, 495 Old Turner St., Blacksburg, VA 0217.

Note. This manuscript was submitted on March 15, 2015; approved on June 3, 2016; published online on August 5, 2016. Discussion period open until January 5, 2017; separate discussions must be submitted for individual papers. This paper is part of the ***Journal of Aerospace Engineering***, © ASCE, ISSN 0893-1321.

Sun 2008, 2010; Unger et al. 2012; Zheng et al. 2013). On the other hand, studies based on robotic flapping devices have provided a deeper understanding of the role of wing flexibility in the context of flapping flight, supporting the results predicted by the aforementioned numerical tools. However, these experimental studies have also shown, in contrast to the computational models, that rigid wings can produce, in some cases, higher lift than flexible ones can (Zhao et al. 2010; Tanaka et al. 2011). Particularly, Zhao et al. (2010) concluded that rigid wings yield the greatest stroke-averaged lift at angles of attack up to 50°, beyond which flexible wings began to dominate.

Currently, the use of unsteady vortex-lattice methods (UVLMs) has been increasing in the study of unsteady problems in which free-wake methods become necessary due to geometric complexity, such as extremely high-altitude long-endurance unmanned aerial vehicles (X-HALE-UAVs), flapping-wing kinematics, morphing wings, and rotorcraft, among others (Wang et al. 2010; Murua et al. 2012; Taha et al. 2012; Obradovic and Subbarao 2011; Wie et al. 2009). Related to flapping-wing aerodynamics, Fritz and Long (2004) implemented the UVLM using object-oriented computing techniques to model the oscillating plunging, pitching, twisting, and flapping motions of a finite-aspect-ratio wing. This work showed that the method is capable of accurately simulating many of the features of complex flapping-wing flight, although the model does not take into account the leading-edge–vortex phenomenon. Stanford and Beran (2010) also used UVLMs to consider the design optimization of a flapping wing in forward flight with active shape morphing, aimed at maximizing propulsive efficiency under lift and thrust constraints. Ghommem et al. (2012) tackled the same problem using global and hybrid optimization techniques. Ghommem used a two-dimensional (2D) version of the UVLM to obtain the hovering kinematics that minimizes the required aerodynamic power under a lift constraint. Willis et al. (2007) presented a simulation tool, *FastAero*, which uses a panel method and an approach based on vortex particles to represent the wake shed from the wing's trailing edge. This approach was demonstrated to be efficient and accurate to study a variety of problems involving unsteady flows and highly flexible lifting surfaces undergoing complex motions.

Taha et al. (2012) established that five terms could be identified as the main contributors to flow quantities during hover. They include the effects due to the wing's translation and rotation, the leading-edge vortices (LEVs), wake capture, viscosity, and added-mass effects. UVLMs capture all of them except the viscous and LEV effects. As shown by the experiments of Dickinson et al. (1999), the viscous effects for the range of Reynolds numbers (75–4,000) of hovering insects can be neglected, which makes the use of UVLMs suitable for the study of flapping-wing aerodynamics.

In this paper, the authors present a new numerical simulation framework to study the production of lift for flapping wings in hover flight under different prescribed deformation patterns. The aerodynamic framework implements (1) a kinematic model that allows imposing different deformation patterns on the wing, such as, torsion, in-plane bending (IPB), and out-of-plane bending (OPB) and (2) a three-dimensional (3D) nonlinear and unsteady version of an aerodynamic model based on UVLM, which was previously modified and extended by the authors of this work (Roccia et al. 2013). This aerodynamic model accounts for all possible aerodynamic interference and allows one to predict (1) the flow field around bodies and lifting surfaces; (2) the spatial-temporal vorticity distribution attached to the solid bodies; (3) the vorticity distribution in wakes emitted from the sharp edges of the wings; (4) the position and shape of wakes; and (5) the unsteady aerodynamic loads acting on the wings.

The remainder of this work is organized as follows. Firstly, the authors give a full description of the kinematic model of the deforming wing. Then a brief description of the current version of UVLM is presented. After that, numerical results of analyzing different deformation patterns are discussed (based on limited experimental data published by biologists and experimentalists) and, finally, some general conclusions on how they affect the lift production are stated. The authors conclude by stating the limitations of the model and how they might be addressed to extend its applicability.

Kinematic Model

The motion of each wing is described using two dextral orthonormal reference frames: (1) a Newtonian or inertial frame $\mathbf{N} = \{\hat{\mathbf{n}}_1, \hat{\mathbf{n}}_2, \hat{\mathbf{n}}_3\}$ and (2) a reference frame fixed to each wing's root in order to facilitate the derivation of the equations $\mathbf{B} = \{\hat{\mathbf{b}}_1, \hat{\mathbf{b}}_2, \hat{\mathbf{b}}_3\}$ for the left wing and $\mathbf{A} = \{\hat{\mathbf{a}}_1, \hat{\mathbf{a}}_2, \hat{\mathbf{a}}_3\}$ for the right wing.

As the wing moves in a 3D space along a predetermined path, its geometry changes according to specific deformation patterns such as spanwise twisting and bending. Therefore, the movement of a material point belonging to the wing can be written as a combination of large rotations and displacements in space (primary motions) and small rotations and displacements associated with elastic deformations (secondary motions), as shown in Fig. 1. The lattice (mesh or grid) is typical of what might be used in UVLM.

The following subsection presents a brief description of the primary motions and a detailed description of the deformation mechanism used to describe secondary motions for the left wing. The kinematic equations for the right wing can be obtained by following the same procedure.

Primary Motions

The wing's orientation at each time step is obtained by specifying the values of three angles (stroke parameters): (1) stroke position angle, $\phi(t)$; (2) stroke deviation angle, $\theta(t)$; and (3) rotation angle, $\psi(t)$. The coordinate transformation from the inertial reference frame $\mathbf{N}$ to the wing-fixed reference frame $\mathbf{B}$ is performed using a (1-3-2) sequence of rotations given by Euler's angles $\phi(t)$, $\theta(t)$ and $\psi(t)$, and represented by the rotation tensor $\mathbf{Q_{BN}}$:$\mathbf{N} \rightarrow \mathbf{B}$.

Fig. 2 shows the angles defined in the preceding paragraph. The stroke position angle is defined by the projection of the longitudinal spanwise axis of the wing $\hat{\mathbf{b}}_2$ onto the stroke plane and the unit vector $-\hat{\mathbf{n}}_2$. The stroke deviation angle is defined as the angle formed by the longitudinal axis of the wing and the stroke plane, and it is considered positive when the wings are above the stroke plane. The rotation angle, $\psi(t)$, is measured on a plane Π, which has an orientation in 3D space that is always normal to the unit vector $\hat{\mathbf{b}}_2$ fixed to the wing; it is defined as the angle formed by the wing's chord and the straight line EE'. Line EE' is fixed to

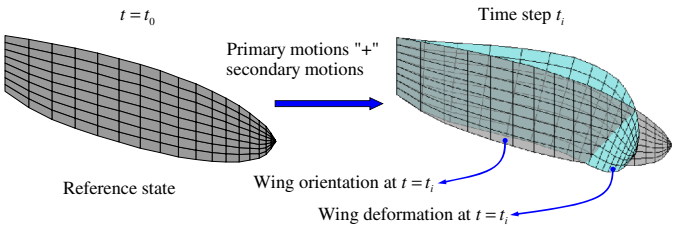

Fig. 1. Wing motion and wing deformation during the stroke cycle

Downloaded from ascelibrary.org by Bruno Antonio Roccia on 08/05/16. Copyright ASCE. For personal use only; all rights reserved.

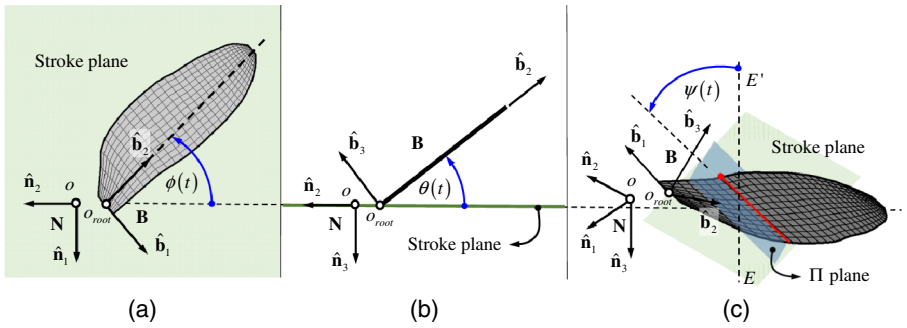

Fig. 2. Stroke parameters, with O_{root} indicatingwing root: (a) stroke-position angle; (b) stroke-deviation angle; (c) rotation angle

the Π plane and coincides with the direction of the unit vector $\hat{\mathbf{b}}_1$ at $t = t_0$. This angle is positive during downstroke.

Roccia et al. (2011) provide a detailed description of the stroke parameters and a full mathematical formulation of the flapping-wing kinematics.

Secondary Motions

In order to impose different deformation patterns on the wing, a "virtual" beam element is defined along the unit vector $\hat{\mathbf{b}}_2$, which provides the necessary ways to bend and twist the wing in a desirable manner. The beam element adopted is an Euler-Bernoulli model, which is considered clamped at the wing root and free to move at the tip. Bending motion in two perpendicular planes (in plane and out of plane) is achieved using expansions in terms of the eigenfunctions, and the spanwise torsion is given by a linear interpolation function. The mechanism used to deform the wing consists of two steps: (1) a deformation pattern is imposed on the virtual beam element (also called elastic axis); and (2) the displacement field is transferred to the rest of the wing by means of an interpolation scheme, which is detailed later in the text.

Figs. 3(a and b) show the location of the virtual beam element inside the wing and the position vector of an arbitrary point belonging to the wing in the undeformed configuration. The point P on the wing's surface and the point P' on the elastic axis lie in the same plane, which is perpendicular to the vector $\hat{\mathbf{b}}_2$ in the undeformed state [Fig. 3(a)]. The cross section of the wing that contains points P and P' is assumed to be rigid, and the position vector of point P relative to point P' is denoted $\mathbf{r}_{P'P}$. The position vector of point P at the undeformed and deformed configurations can be written, respectively, as follows:

$$\mathbf{R}_P = \mathbf{R}_{\text{root}} + \mathbf{r}_{P'} + \mathbf{r}_{P'P}, \qquad \tilde{\mathbf{R}}_P = \mathbf{R}_{\text{root}} + \mathbf{r}_{P'} + \mathbf{u}_{P'} + \mathbf{T}\mathbf{r}_{P'P} \tag{1}$$

where $\mathbf{R}_{\text{root}}$ = position vector of the origin of the reference frame $\mathbf{B}$ fixed to the wing root; $\mathbf{r}_{P'}$ = position vector of the point P' on the elastic axis in the undeformed configuration; $\mathbf{u}_{P'}$ = elastic displacement vector associated with point P'; and $\mathbf{T}$ = infinitesimal rotation tensor (Baruh 1999).

Then the displacement vector of point P is obtained as the difference between the position vector of P at the deformed configuration and the position vector of P at the undeformed configuration:

$$\tilde{\mathbf{R}}_P - \mathbf{R}_P = \mathbf{u}_{P'} + (\mathbf{T} - \mathbf{1}_3)\mathbf{r}_{P'P} \tag{2}$$

where $\mathbf{1}_3$ = second-order identity tensor.

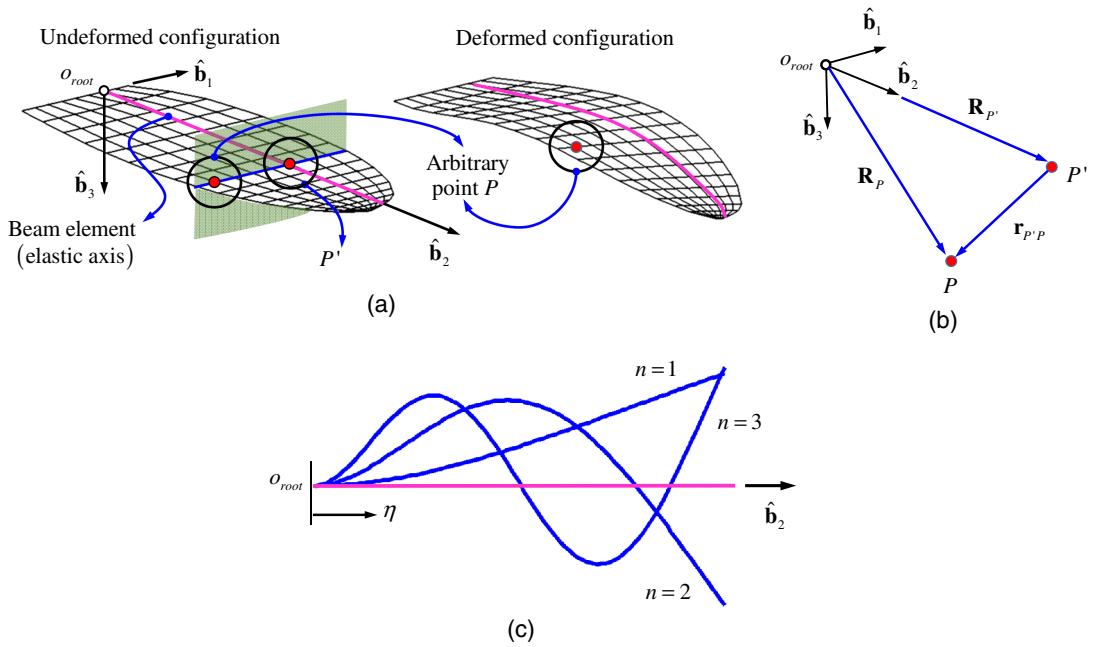

Fig. 3. (a) Undeformed and deformed configurations of the wing; (b) definition of the position vector of point P at the undeformed configuration; (c) eigenfunctions for a clamped-free Euler-Bernoulli beam

Downloaded from ascelibrary.org by Bruno Antonio Roccia on 08/05/16. Copyright ASCE. For personal use only; all rights reserved.

After some algebraic manipulations and by expressing the result in a given basis, the position vector of P at the deformed configuration can be expressed as

$$\{\tilde{\mathbf{R}}_P\} = \{\mathbf{R}_P\} + \{\mathbf{u}_{P'}\} - [\bar{\mathbf{r}}_{P'P}]\{\boldsymbol{\theta}\} \tag{3}$$

where $\{\boldsymbol{\theta}\} = (\theta_1, \theta_2, \theta_3)^T$ = small rotations due to the elastic axis deformation; and $[\bar{\mathbf{r}}_{P'P}]$ = skew-symmetric matrix given by

$$[\bar{\mathbf{r}}_{P'P}] = \begin{bmatrix} 0 & -r_3 & r_2 \\ r_3 & 0 & -r_1 \\ -r_2 & r_1 & 0 \end{bmatrix} \tag{4}$$

where r_1, r_2, and r_3 = components of vector $\{\mathbf{r}_{P'P}\}$—that is, $\{\mathbf{r}_{P'P}\} = (r_1, r_2, r_3)^T$.

Each of the components of the elastic displacement vector $\{\mathbf{u}_{P'}\} = (u_1, u_2, u_3)^T$ is expressed as the product of an eigenfunction, $S(\eta)$ and a generalized coordinate $p(t)$:

$$u_i(\eta; t) = S_i(\eta) p_i(t) \quad \text{for } i = 1,2,3 \tag{5}$$

The eigenfunctions $S_i(\eta)$ (for $i = 1,2,3$) are obtained from the analytical solution of the differential equation that governs the free-vibration problem of an Euler-Bernoulli beam with clamped-free boundary conditions (Karnovsky and Lebed 2000) [Fig. 3(c)]. The component $u_2(\eta; t)$, which accounts for the axial displacement, is identically zero for all t. The generalized coordinates $p_i(t)$ are expressed in terms of harmonic functions. The elastic rotations $\theta_1(\eta; t)$ and $\theta_3(\eta; t)$ are obtained by evaluating the partial derivative of the displacement's components $u_3(\eta; t)$ and $u_1(\eta; t)$ with respect to η, respectively. Moreover, the rotation $\theta_2(\eta; t)$ is interpolated by a linear function and represents the twist angle around the elastic axis:

$$\begin{aligned} \theta_1(\eta; t) &= \partial_\eta u_3(\eta; t) = d_\eta[S_3(\eta)] p_3(t), \\ \theta_2(\eta; t) &= S_{\text{twist}}(\eta) p_{\text{twist}}(t) = \frac{\eta}{R} p_{\text{twist}}(t) \quad \text{and} \\ \theta_3(\eta; t) &= -\partial_\eta u_1(\eta; t) = -d_\eta[S_1(\eta)] p_1(t) \end{aligned} \tag{6}$$

where ∂_η = partial derivative with respect to η; d_η = total derivative with respect to η; $p_{\text{twist}}(t)$ = generalized elastic coordinate that regulates the time variation of the wing torsion; and R = wing span.

This formulation allows one to rewrite the elastic displacement vector of an arbitrary point P on the wing as

$$\{\mathbf{u}_P\} = \{\mathbf{u}_{P'}\} - [\bar{\mathbf{r}}_{P'P}]\{\boldsymbol{\theta}\} = [\mathbf{N}(\eta)]\{\mathbf{p}(t)\} \tag{7}$$

where

$$[\mathbf{N}(\eta)] = \begin{bmatrix} S_1(\eta) & 0 & 0 \\ -r_1 d_\eta[S_1(\eta)] & 0 & 0 \\ 0 & -r_1 S_{\text{twist}}(\eta) & S_3(\eta) \end{bmatrix} \quad \text{and}$$

$$\{\mathbf{p}(t)\} = [p_1(t), p_{\text{twist}}(t), p_3(t)]^T \tag{8}$$

Here $[\mathbf{N}(\eta)]$ = matrix of shape functions; and $\{\mathbf{p}(t)\}$ = array containing the elastic generalized coordinates.

The velocity of P in the $\mathbf{N}$ reference frame can be obtained by evaluating the total time derivative of the position vector $\tilde{\mathbf{R}}_P$ performed by an observer fixed to the inertial reference frame $\mathbf{N}$:

$$\dot{\tilde{\mathbf{R}}}_P = \dot{\mathbf{R}}_P + \dot{\mathbf{Q}}_{\mathbf{NB}}\mathbf{u}_P + \mathbf{Q}_{\mathbf{NB}}\dot{\mathbf{u}}_P \tag{9}$$

where the dot = ${}^N d/dt$; and $\mathbf{Q}_{\mathbf{NB}}$:$\mathbf{B} \rightarrow \mathbf{N}$ = rotation tensor from the $\mathbf{B}$ reference frame to the $\mathbf{N}$ reference frame and is obtained as the inverse of tensor $\mathbf{Q}_{\mathbf{BN}}$.

Finally, Eq. (9) can be expressed as follows:

$$\mathbf{V}_P = \dot{\tilde{\mathbf{R}}}_P = \dot{\mathbf{R}}_P + \mathbf{Q}_{\mathbf{NB}}(\bar{\boldsymbol{\omega}}\mathbf{u}_P + \dot{\mathbf{u}}_P) \tag{10}$$

where $\bar{\boldsymbol{\omega}}$ = skew-symmetric tensor associated with the axial vector ${}^N\boldsymbol{\omega}^B$; and ${}^N\boldsymbol{\omega}^B$ = angular velocity vector for primary motions, which is found using the angular velocity addition theorem and the stroke parameters detailed previously.

Aerodynamic Model

Wings are considered surfaces. The boundary layers on the upper and lower sides of these surfaces are merged into a single layer of vorticity to form a single vortex sheet, referred to as a lifting surface. Here the terms *lifting surface*, *vortex sheet*, and *wing* may be used interchangeably. A lifting surface is bound to, and hence moves and deforms with, a wing. As a result of prescribing the motion of a lifting surface, there is a discontinuity in the pressure across it when the distribution of vorticity in it is determined by imposing the no-penetration condition on it. This discontinuity produces the aerodynamic forces.

Wakes are also vortex sheets. They form along those edges of the lifting surfaces where the pressure jump across the surface is made to vanish, a requirement often labeled the unsteady Kutta condition. Making the pressure continuous requires vorticity to be "shed" (emitted) from the lifting surface. After being shed, vorticity moves downstream with the fluid particles so that the pressure in the wake remains continuous. The distribution and position of vorticity in the force-free wake are determined as part of the solution.

On the other hand, the additional leading-edge separation (LEV) plays a fundamental role in flight at small scales (flying insects, rotating seeds, and small birds); this phenomenon explains the high lift generated by these natural fliers (Pitt Ford and Babinsky 2013; Lentink and Dickinson 2009). Although an integral aerodynamic study of MAV-like flapping wings should include a LEV model, the numerical framework presented here does not take into account this phenomenon. Some proofs were carried out by implementing the on/off mechanism proposed by Roccia et al. (2013) to account for the leading-edge separation, but the authors found significant numerical instabilities when the wing was allowed to deform according to prescribed deformation patterns presented in this work. On this basis, it was decided to neglect the LEV phenomenon (being aware of the restriction that it supposes) and focus on how these deformation patterns affect lift production.

The proposed model considers a flow of an incompressible fluid characterized by a very high Reynolds number. The governing equation is the well-known Laplace's equation of continuity for incompressible and nonrotational flows. The velocity at point $\mathbf{x}$ in the flow field, $\mathbf{V}(\mathbf{x}; t)$, associated with a straight vortex-line segment is given by the Biot-Savart law:

$$\mathbf{V}(\mathbf{x}; t) = \frac{\Gamma(t)}{4\pi} \frac{\omega(\mathbf{x}; t) \times \mathbf{x}_1}{\|\omega(\mathbf{x}; t) \times \mathbf{x}_1\|_2^2 + (\delta\|\omega\|_2)^2} [\omega(\mathbf{x}; t) \cdot (\hat{\mathbf{e}}_1 - \hat{\mathbf{e}}_2)] \tag{11}$$

where $\mathbf{x}_1$ and $\mathbf{x}_2$ = position vectors of the point where the velocity is being computed relative to the ends of the straight vortex segment; $\hat{\mathbf{e}}_1$ and $\hat{\mathbf{e}}_2$ = unit vectors parallel to $\mathbf{x}_1$ and $\mathbf{x}_2$; $\boldsymbol{\omega} = \mathbf{x}_1 - \mathbf{x}_2$; and δ = cutoff radius (Roccia et al. 2013; Van Garrel 2003) used to eliminate the singularity at points on the vortex line.

In the unsteady vortex-lattice method, a lattice of short, straight vortex segments of circulation $\Gamma_i(t)$ replaces the bound-vortex sheets. These segments divide the surface of the insect's wings into

Downloaded from ascelibrary.org by Bruno Antonio Roccia on 08/05/16. Copyright ASCE. For personal use only; all rights reserved.

a number of area elements (panels). The model is completed by joining the free-vortex lines, representing the free-vortex sheets, to the bound-vortex lattice along the edges of separation, such as the trailing edges and wingtips.

Unlike aircraft wings or helicopter blades, where the trailing edge and wingtip are well defined, in MAV-like flapping wings inspired by biology, such as those discussed in this paper, the trailing edge and wingtip are not well demarcated and merge into a single sharp edge (with high curvature) where vortex shedding takes place. With this in mind, the shedding zone is defined from the wing root to the tip of the insect wing.

The governing equation of the problem has the following boundary conditions:

- Regularity at infinity, which requires that all disturbances due to a moving body in a fluid, initially at rest, decay away from the body and its wakes; and
- The no-penetration condition, which requires that the normal component of the fluid's velocity relative to the wing's moving surface be zero:

$$(\mathbf{V}_{\text{fluid}} - \mathbf{V}_{\text{lifting surfac}}) \cdot \hat{\mathbf{n}} = 0 \rightarrow (\mathbf{V}_\infty + \mathbf{V}_B + \mathbf{V}_W - \mathbf{V}_P) \cdot \hat{\mathbf{n}} = 0 \quad \text{everywhere on the lifting surfaces} \tag{12}$$

where $\mathbf{V}_\infty$ = free-stream velocity, as mentioned before; $\mathbf{V}_B$ and $\mathbf{V}_W$ = velocities associated with the vorticity in the lifting surfaces and wakes; $\mathbf{V}_P$ = velocity of the body's surface defined in Eq. (10); and $\hat{\mathbf{n}}$ = unit vector normal to the lifting surface.

Because there are a finite number of panels, and hence unknown circulations, Eq. (12) can only be satisfied at a finite number of points; here it is at one point in each panel, called the control point.

Eq. (12) is used to compute $\mathbf{V}_B$, which is expressed in terms of the unknown values for the loop vortex circulations $G_j(t)$ and the aerodynamic influence coefficients $A_{ij}(t)$ (Konstandinopoulos 1981; Preidikman 1998).

Once the resulting linear system is solved for $G_j(t)$, the distribution of vorticity in the lifting surface is known at t; then the pressure jump across the lifting surface, $\Delta p(\mathbf{x};t)$, is calculated by means of the unsteady Bernoulli's equation:

$$\partial_t \varphi(\mathbf{x};t) + \frac{1}{2}\mathbf{V}(\mathbf{x};t) \cdot \mathbf{V}(\mathbf{x};t) + \frac{p(\mathbf{x};t)}{\rho} = H(t) \tag{13}$$

where ∂_t = partial derivative with respect to time at a fixed location in an inertial reference frame; $p(\mathbf{x};t)$ = unknown pressure; ρ = constant density of the fluid; and $H(t)$ has the same value at every point in the flow field at any instant.

Details of the treatment of each term in Eq. (13) and the full formulation of the unsteady vortex-lattice method are given by Konstandinopoulos (1981), Preidikman (1998), Preidikman and Mook (2000), and Roccia et al. (2013). The last reference contains all the extensions needed to attack the problem of flapping wings.

Numerical Results

In this section, the authors present some results obtained with the present numerical model. The computer code was written in Intel Corporation (2003) and compiled on a Windows platform. Automatic optimization options, which are specific for Intel processors, were used to enhance performance. For all cases, the code was run on a desktop computer with an i7 processor (Intel, Santa Clara, CA), RAM DDR3 of 4 GB, and a hard disk of 2 TB.

Validation of the aerodynamic simulation framework used in this work was formerly addressed in Roccia et al. (2013). However, some of these validations are in the next subsection for convenience. Finally, the authors investigate the influence of different patterns of deformation on the lift and compare them against a rigid-wing model.

Validations

In this subsection, two well-known problems documented in the literature are presented. The first one is the case of a flapping/twisting wing, and the second one is the case of a hovering wing.

Flapping/Twisting Wing

Neef and Hummel (2001) considered a rectangular wing of $AR = 8$, a NACA 0012 (National Advisory Committee for Aeronautics) profile, a flapping amplitude of 15°, and a reduced frequency $k = 0.1$ (k is defined as $\omega c/2V_\infty$, where ω = the flapping frequency; c = the wing chord; and V_∞ = the free-stream velocity magnitude). The sinusoidal flapping motion has an out-of-phase twisting rotation around the leading edge superimposed linearly along the span, from 0° at the root to 4° at the tip. The flapping period, T_f, was discretized into 40 equal time steps.

To describe the flapping/twisting motion of Neef's and Hummel's wing, the authors use another kinematic model that allows one to prescribe only twist deformation by means of finite rotations. The systems **B** and **C** were located at the leading edge, and the rotation matrix from **C** to **B** is defined as follows:

$$[\mathbf{Q}_{\text{BC}}] = \begin{bmatrix} \cos\beta & 0 & -\sin\beta \\ 0 & 1 & 0 \\ \sin\beta & 0 & \cos\beta \end{bmatrix} \tag{14}$$

The angle β determines the orientation of System **C** with respect to System **B**; it is associated with the twisting motion. The location of the origin of System **C** along the span is determined by ζ, a function of position along the span. Fig. 4 shows the location of the reference systems. The angles that describe the motion of the wing are expressed as follows:

$$\beta = -\left(\frac{4\pi}{180}\right)\left(\frac{2\zeta}{b}\right)\sin(\omega t) \tag{15}$$

Fig. 5(a) provides the kinematic pattern. Fig. 5(b) provides two sets of comparative results for the time-dependent lift coefficient of the flapping/twisting wing described previously with its fixed root chord inclined at two constant angles of attack (α_{root}) of 0° and 4°. The results of Neef and Hummel were computed by solving the Euler equations, and the results of Stanford and Beran (2010), using their own version of the unsteady vortex-lattice method to solve for the flow past a flat plate. Agreement among the three sets of results is excellent. The minor differences between the lift computed by Stanford and Beran and the one calculated in this work lie in the specification of some user-defined parameters, such as the

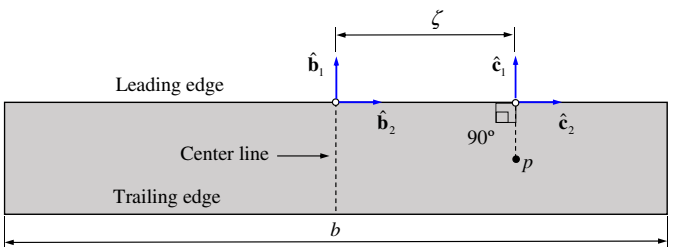

Fig. 4. Location of the reference systems on the flapping/twisting wing

Downloaded from ascelibrary.org by Bruno Antonio Roccia on 08/05/16. Copyright ASCE. For personal use only; all rights reserved.

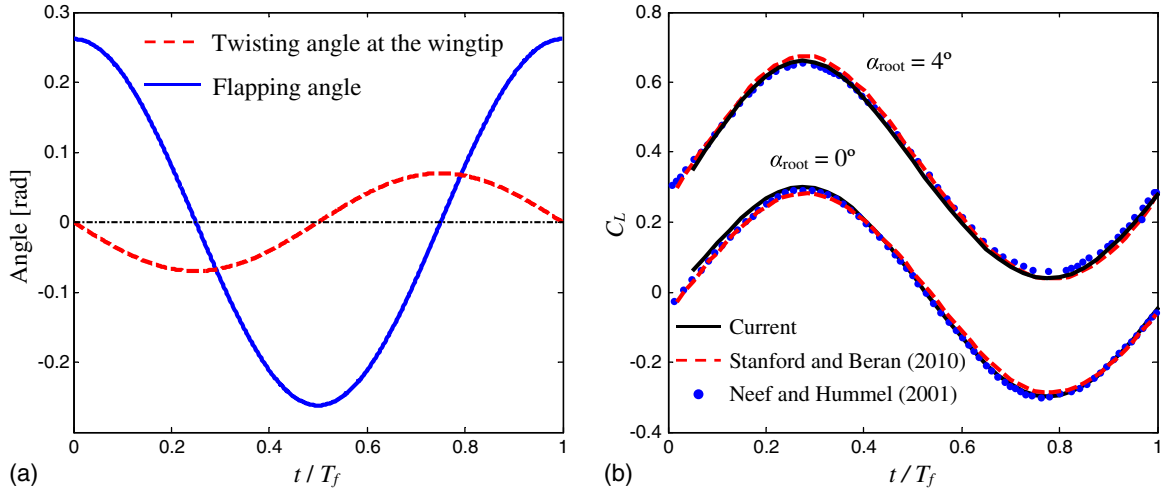

Fig. 5. (a) Flapping and twisting motions (data from Neef and Hummel 2001); (b) comparison of the current lift coefficient with previous numerical simulations during one cycle

cutoff radius and differences in the two versions of Bernoulli's equation. In this numerical experiment, the wing-tip vortex system was omitted.

Hovering Wing

Here the lift obtained with the present numerical simulation is compared with the experimental data of Dickinson et al. (1999), whose experiment was performed with a dynamically scaled model of a *Drosophila melanogaster*, dubbed Robofly. The motion of the model's two wings was driven by an assembly of six computer-controlled stepper motors so that each wing was capable of rotational motion about three axes. The wings were immersed in a 1×2-m cross-section tank filled with mineral oil with density $\rho = 880$ kg/m^3 and kinematic viscosity $\nu = 115\,cSt$, where centistokes (cSt) is the unit of kinematic viscosity.

The wing performed an insect-like flapping motion at a frequency of $n_f = 0.145$ Hz, with its tip tracing out a flat figure-of-eight. The kinematic pattern consisted of a stroke amplitude of 160° and an angle of attack at midstroke of 40° for both upstroke and downstroke. Fig. 6(a) shows the wing's kinematics for a pattern in which the rotation precedes the reversal stroke by 8% of the wing-beat cycle. Fig. 6(b) compares the lifts obtained in the present simulation and in the experiments.

The present results are very encouraging because they agree more closely with those of Dickinson et al. than the results reported in two previously published comparisons: the computational fluid dynamics (CFD) study by Sun and Tang (2002), and the 2D aerodynamic model developed by Ansari et al. (2006a, b). These results are significant because they justify use of the nonlinear-unsteady vortex-lattice method to characterize the 3D aerodynamic behavior of insects executing different maneuvers.

To further justifyusing a modified version of the unsteady vortex-lattice method applied to flapping wings, the reader can consult the work of Roccia et al. (2013).

Case Studies

In this subsection, the aerodynamic framework developed is used to analyze how the lift force changes because of the imposition of different deformation patterns on a flapping wing.

According to observations performed by Ellington (1984) and Ennos (1989) on the wing kinematics of hoverflies, involving

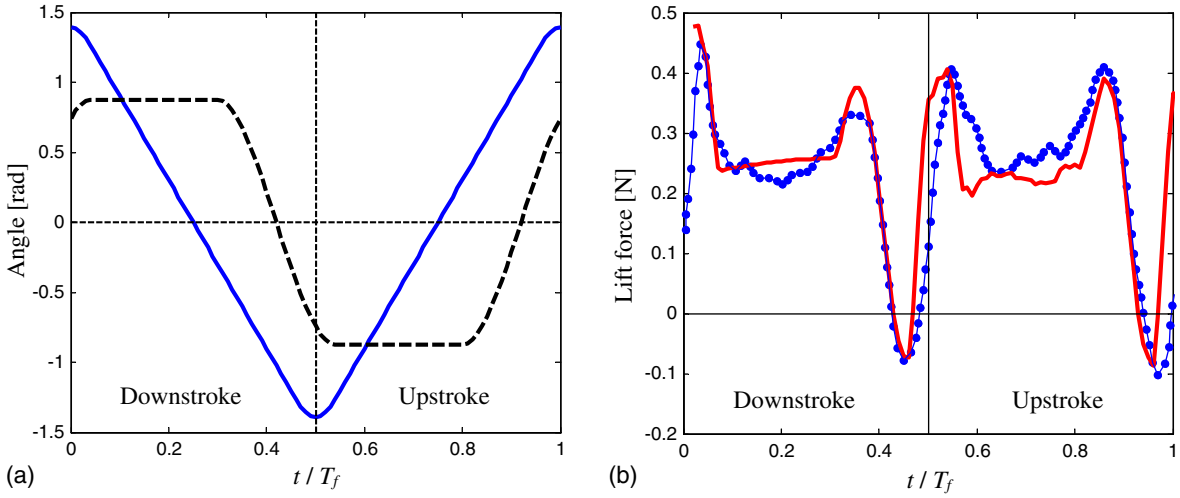

Fig. 6. (a) Wing kinematics (solid line for the stroke angle; broken line for the angle of rotation); (b) comparison of the present numerical results (solid line) with the experimental measurements for the Robofly apparatus (circles)

Downloaded from ascelibrary.org by Bruno Antonio Roccia on 08/05/16. Copyright ASCE. For personal use only; all rights reserved.

quantitative measurements of wing-tip paths and qualitative descriptions of wing deformation, twist is increased from zero to some constant value at the beginning of either downstroke or upstroke and kept constant during the midportion of the half-stroke. Near the end of the half-stroke, the twist starts decreasing until it becomes zero at the end of the half-stroke. Ellington and Ennos also detected that the geometric angle of attack varies approximately linearly along the wing span (termed *linear twist*). Walker et al. (2009a) showed that twist is approximately constant in the mid half-stroke, similar to that described by Ellington and Ennos, but around the stroke reversal the twist is much larger than at the mid half-stroke. On the basis of these observations, it was assumed in the current study that the twist deformation varies linearly along the wing span. The temporal evolution of the spanwise twist through the stroke cycle can be approximately matched using harmonic functions. The effect described by Walker and colleagues on the reversal stroke might be partially modeled by changing the phase angle between the twist deformation and the wing motion.

Because of the lack of data on how flying insects bend their wings during the flapping cycle, the authors propose, as a first approach, to use eigenfunctions to prescribe the bending along the wing span (normal and tangential to the wing chord) and harmonic functions to account for the time variation during the stroke cycle.

To carry out such analyses, the robofly kinematics shown in Fig. 6(a) and an example of the actual kinematics of a fruit fly in hover (Bos et al. 2007) were used. In all cases, the wing geometry, the wing-beat frequency, and the fluid density correspond to the experiment performed by Dickinson et al. which was briefly described previously.

The deformation patterns investigated in this section are (1) spanwise twist; (2) out-of-plane bending (normal to the wing chord); and (3) in-plane bending (tangential to the wing chord). Finally, the authors present a case that combines all the aforementioned deformation patterns in order to increase lift during the entire stroke cycle.

The generalized coordinates $p_i(t)$ for $i = 1, \text{twist}, 3$, which control temporal variation in the bending and wing torsion, are specified by the following harmonic function:

$$p_i(t) = a_i \sin(\omega_i t + \beta_i) \text{ for } i = 1, \text{twist}, 3 \tag{16}$$

where ω_i = circular frequencies; β_i = phase angles between the temporal coordinates $p_i(t)$ and the stroke position angle; and a_i = deformation amplitudes associated with the wingtip. To obtain the influence of the deformation pattern on the lift, a parametric study varying the phase angle β_i was performed; specifically, three cases were considered: (1) the imposition of the deformation preceding the reversal stroke (advanced deformation pattern, $0 < \beta_i \leq 0.5\pi$); (2) the deformation occurring symmetrically with respect to the reversal stroke (symmetrical deformation pattern, $\beta_i = 0$); and (3) the deformation is delayed with respect to the reversal stroke (delayed deformation pattern, $-0.5\pi \leq \beta_i < 0$). The parameters in Eq. (16) are given in Table 1 for the three different deformation patterns analyzed.

As mentioned previously, the spatial variation associated with the spanwise-twist deformation is linear, and both out-of-plane and in-plane bending deformations are described by the eigenfunction corresponding to the fundamental free-vibration mode of a Euler-Bernoulli beam perfectly clamped at one end and free to move at the other [Fig. 3(c)].

The results in the following subsections are from numerical experiments that were carried out on an aerodynamic mesh composed of 200 panels per wing and a stroke cycle discretized into 100 time-steps. For reasons concerning the limitations of the current aerodynamic model, only the first stroke cycle is analyzed. A typical run of the code for the case studies presented in this section was approximately 55 min.

A cutoff radius value of $\delta = 0.15$ (15%) was used to compute the influence of the trailing-edge vortex (TEV) over itself and over the bounded-sheet. Cutoff radius values smaller than 15% produce too much noise on lift forces. It is noteworthy that the ad hoc procedure in this paper uses an embedded cutoff. Furthermore, the modified singular core $\mathbf{K}(\mathbf{R} - \mathbf{R}_0; \delta)$ in Eq. (11) depends on the magnitude of the vorticity segment. This feature makes this technique well suited to treat problems involving structures undergoing complex motions.

Twisting

Fig. 7 shows how the lift is affected by the twist of the wing for different values of the phase angle. The shaded region around the lift for the rigid wing represents the maximum possible deviation that can be achieved by varying the phase angle β_{twist} between -0.5π and 0.5π.

Essentially, the twist angle increases or decreases the effective angle of attack, which directly affects the aerodynamic forces. The timing between the stroke-position angle and the twist angle is primarily responsible for the changes observed in Figs. 7(a and b). For the robofly kinematics and an advanced twisting pattern, the most noticeable change in the lift occurs in rotational phases (pronation/supination) [Fig. 7(a)]. Specifically, this pattern increases lift during the reversal stroke and decreases it during downstroke/upstroke. Whereas the phase angle β_{twist} varies from 0.5π to -0.5π, the effect is completely reversed to obtain, for a delayed twisting pattern, an increase in lift during downstroke/upstroke and almost no change during the rotational phases.

A similar analysis using the real kinematics of a fruit fly and an advanced twisting pattern reveals substantially different behavior

Table 1. Summary of Deformation Pattern Configurations

Pattern	Phase angle, β_i (rad)	Circular frequency, ω_i (rad/s)	Amplitude, a_i	Denomination
Twisting (i = twist)	-0.5π	$2\pi n_f$	10°	Delayed twisting pattern
	0.0	$2\pi n_f$	10°	Symmetrical twisting pattern
	0.5π	$2\pi n_f$	10°	Advanced twisting pattern
Out-of-plane bending ($i = 3$)	-0.5π	$2\pi n_f$	$0.1R$	Delayed OPB pattern
	0.0	$2\pi n_f$	$0.1R$	Symmetrical OPB pattern
	0.5π	$2\pi n_f$	$0.1R$	Advanced OPB pattern
In-plane bending ($i = 1$)	-0.5π	$2\pi n_f$	$0.1R$	Delayed IPB pattern
	0.0	$2\pi n_f$	$0.1R$	Symmetrical IPB pattern
	0.5π	$2\pi n_f$	$0.1R$	Advanced IPB pattern

Note: IPB = in-plane bending; $n_f = 0.145$ Hz [see the experiment carried by Dickinson et al. (1999)]; $R = 19$ cm; OPB = out-of-plane bending.

Downloaded from ascelibrary.org by Bruno Antonio Roccia on 08/05/16. Copyright ASCE. For personal use only; all rights reserved.

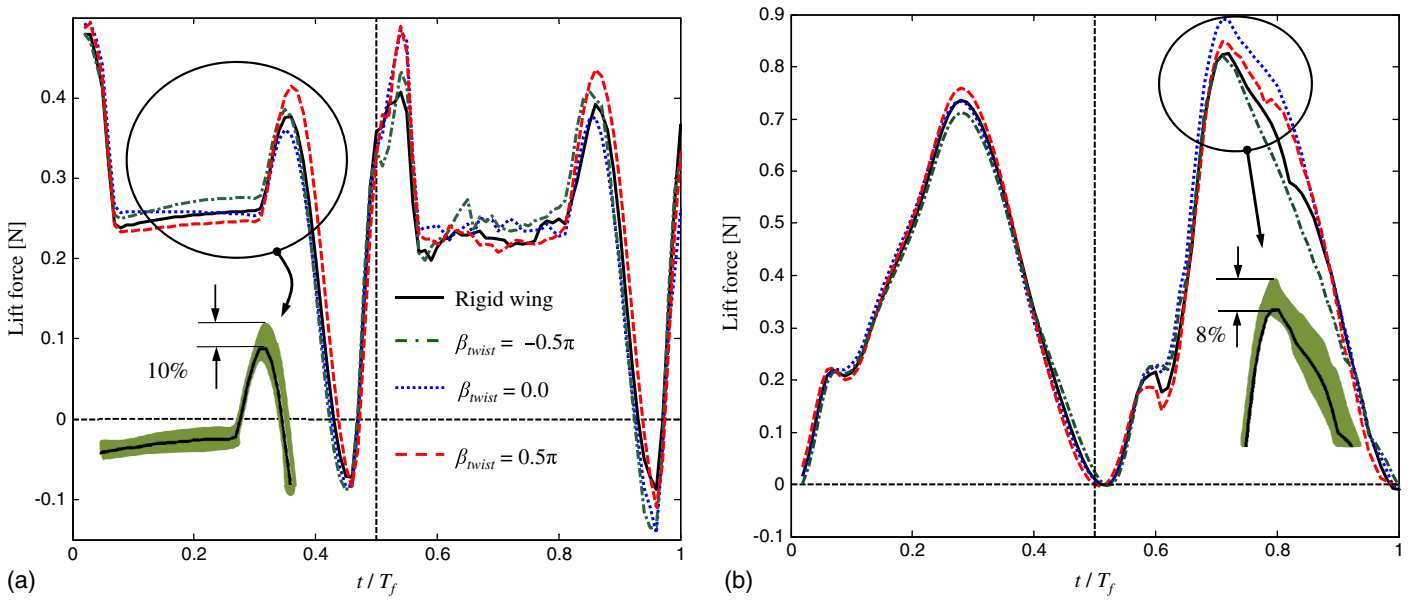

Fig. 7. Influence of twist angle on lift for (a) robofly kinematics; (b) real kinematics of a fruit fly in hover

and less influence of twist on lift. Nevertheless, one can see an increase in lift over the upstroke; elsewhere in the stroke cycle, lift is almost not affected by twist.

For the cases presented in this subsection, the influence of the wing's twist on mean lift is very small. However, this fact suggests that a mechanism to twist the wing could be used in devices such as MAV-like flapping wings in order to maximize lift at certain moments in the stroke cycle.

Out-of-Plane Bending

In this subsection, the effect of out-of-plane bending on lift is analyzed. To perform these analyses, two different deformation patterns related to the imposition of bending are considered. They differ only in the sign of the wingtip displacement relative to the wing's motion. In Fig. 8, the two configurations for out-of-plane bending (OPB1 and OPB2) are shown.

In the OPB1 configuration, the wingtip displacement is opposite to the wing motion [Fig. 8(a)]; in contrast, in the OPB2 configuration the wingtip displacement is in the same direction as the wing motion [Fig. 8(b)]. The analysis presented in this subsection was performed for both configurations, OPB1 and OPB2, and for three different values of the phase angle (Table 1).

The analyzed cases show that OPB either increases (OPB1) or decreases (OPB2) lift throughout the stroke cycle (Fig. 9). Although the numerical experiments carried out here are restricted to small deformations, because of the adopted kinematic model, a significant increment in the mean value of the lift can be observed (Table 2). Moreover, the results for the cases studied show that a deformation pattern such as OPB acts globally over the entire stroke cycle by increasing or decreasing lift; this is substantially different from twisting, which acts locally over specific areas of the stroke cycle.

In Table 2, the results show that the configurations (OPB1, $\beta_3 = 0.5\pi$) and (OPB2, $\beta_3 = -0.5\pi$) produce maximum lift for both real and robofly kinematics. The values in parentheses indicate the percentage difference with respect to the rigid wing. Furthermore, the configuration (OPB2, $\beta_3 = -0.5\pi$) produces identical results to the configuration (OPB1, $\beta_3 = 0.5\pi$). This is because the deformation patterns specified by them are exactly the same. Also, the lift curves computed with phase angles -0.5π and 0.5π generate a boundary that contains all lift curves associated with a phase angle in the interval $[-0.5\pi, 0.5\pi]$, as can be seen in shaded region in Figs. 9(a–d)].

In-Plane Bending

In this subsection, the effects of in-plane bending on lift are studied. Two deformation patterns are analyzed, as before, related to the imposition of the displacement sign at the wingtip relative to the wing motion (Fig. 10).

The IPB1 configuration imposes a positive displacement at the wingtip (in the direction of the unit vector $\hat{\mathbf{b}}_1$) during the downstroke and a negative value during the upstroke. Conversely, the

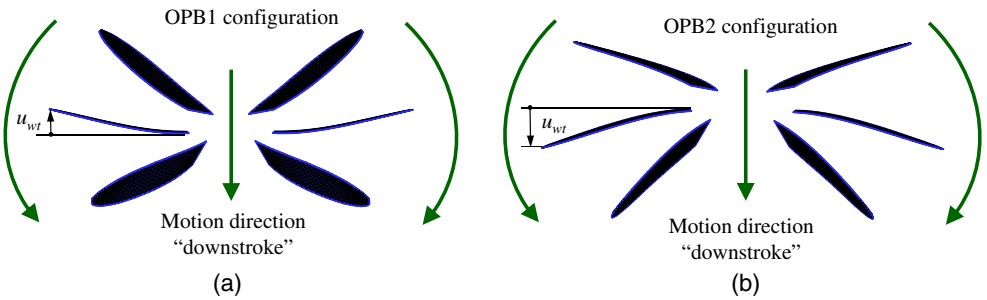

Fig. 8. Out-of-plane bending configurations: (a) OPB1 configuration; (b) OPB2 configuration (u_{wt} is the displacement at the wingtip)

Downloaded from ascelibrary.org by Bruno Antonio Roccia on 08/05/16. Copyright ASCE. For personal use only; all rights reserved.

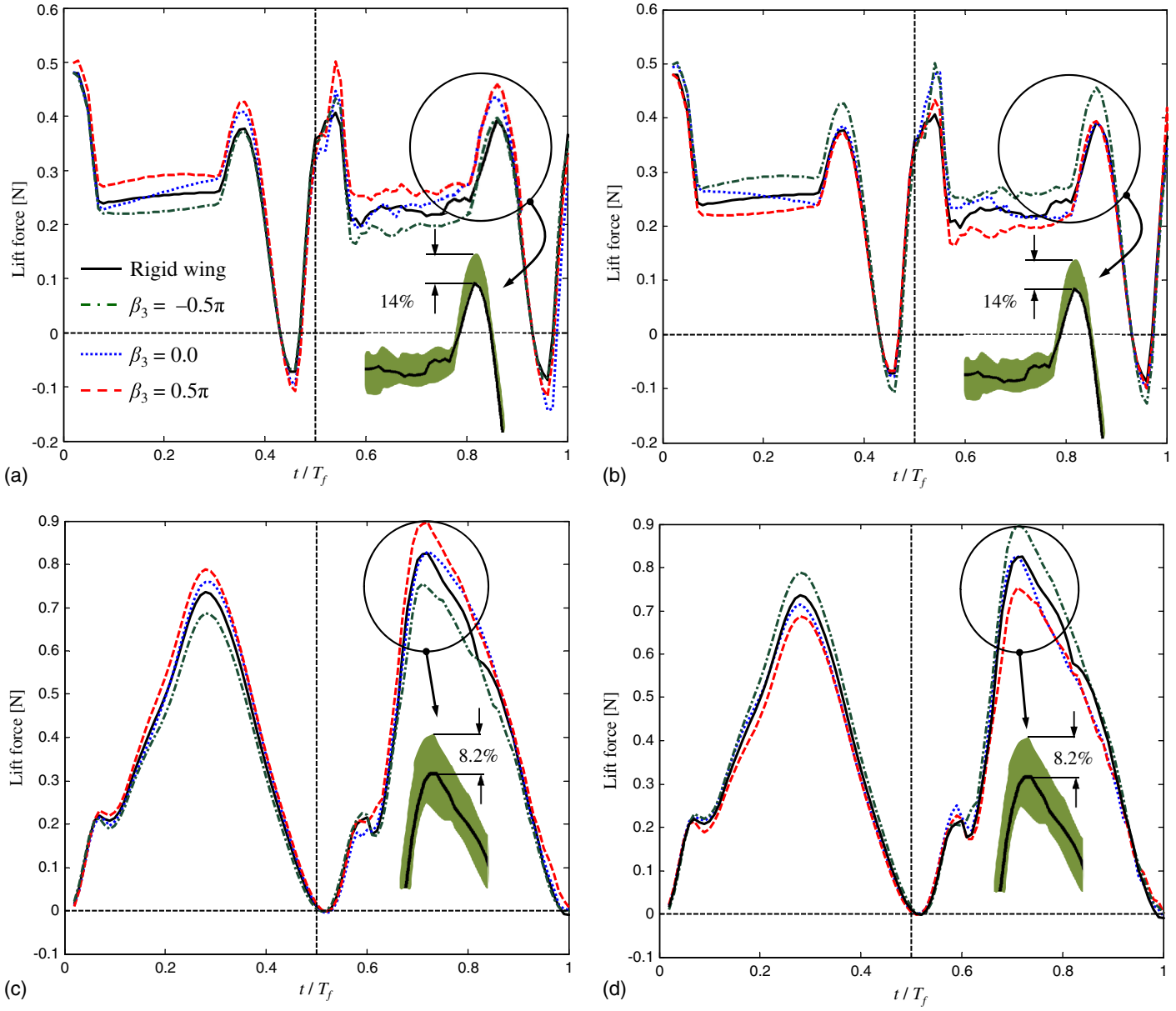

Fig. 9. Influence of out-of-plane bending on lift: (a) robofly kinematics for OPB1; (b) robofly kinematics for OPB2; (c) real kinematics for OPB1; (d) real kinematics for OPB2

Table 2. Mean Lift—Out-of-Plane Bending

Kinematics	Phase angle, β_3	Mean lift (N) OPB1 configuration	Mean lift (N) OPB2 configuration
Robofly	Rigid wing	0.24056	—
	0.5π	0.26760 (+11.20%)	0.22419 (−6.80%)
	0.3π	0.26619 (+10.65%)	0.23264 (−3.30%)
	0	0.24355 (+1.35%)	0.24614 (+2.30%)
	-0.3π	0.23030 (−4.30%)	0.26257 (+9.10%)
	-0.5π	0.22700 (−5.70%)	0.26705 (+11.00%)
Real	Rigid wing	0.37642	—
	0.5π	0.40916 (+8.70%)	0.35000 (−7.01%)
	0.3π	0.40957 (+8.80%)	0.35064 (−6.85%)
	0	0.38565 (+2.50%)	0.36815 (−2.20%)
	-0.3π	0.36004 (−4.35%)	0.39282 (+4.35%)
	-0.5π	0.34946 (−7.20%)	0.40645 (+8.00%)

IPB2 configuration imposes a negative displacement at the wingtip during the downstroke and a positive value during the upstroke. Lift curves for both IPB1 and IPB2 are presented in Fig. 11.

The effects on lift after imposing in-plane bending are similar to those observed after applying twist (Fig. 11). On the one hand, using the robofly kinematics and the configuration (IPB1, $\beta_1 = 0.5\pi$), the lift slight decreases during the downstroke and slightly increases at the beginning of pronation. In the second half-stroke, the lift slightly increases during the upstroke and supination also [Figs. 11(a and b)]. The configuration (IPB2, $\beta_1 = -0.5\pi$) produces results identical to the results for configuration (IPB1, $\beta_1 = 0.5\pi$) for the same reasons discussed for the out-of-plane bending.

On the other hand, the real wing motion of a fruit fly in hover produces almost the same effects on lift as observed for the robofly kinematics. Some differences can be distinguished in the rotational phases pronation/supination at $t = 0.1T_f$ and $t = 0.6T_f$, where the

Downloaded from ascelibrary.org by Bruno Antonio Roccia on 08/05/16. Copyright ASCE. For personal use only; all rights reserved.

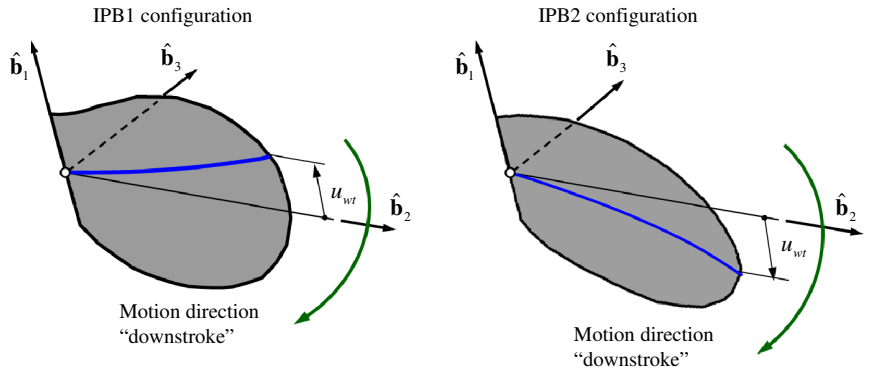

Fig. 10. In-plane bending configurations

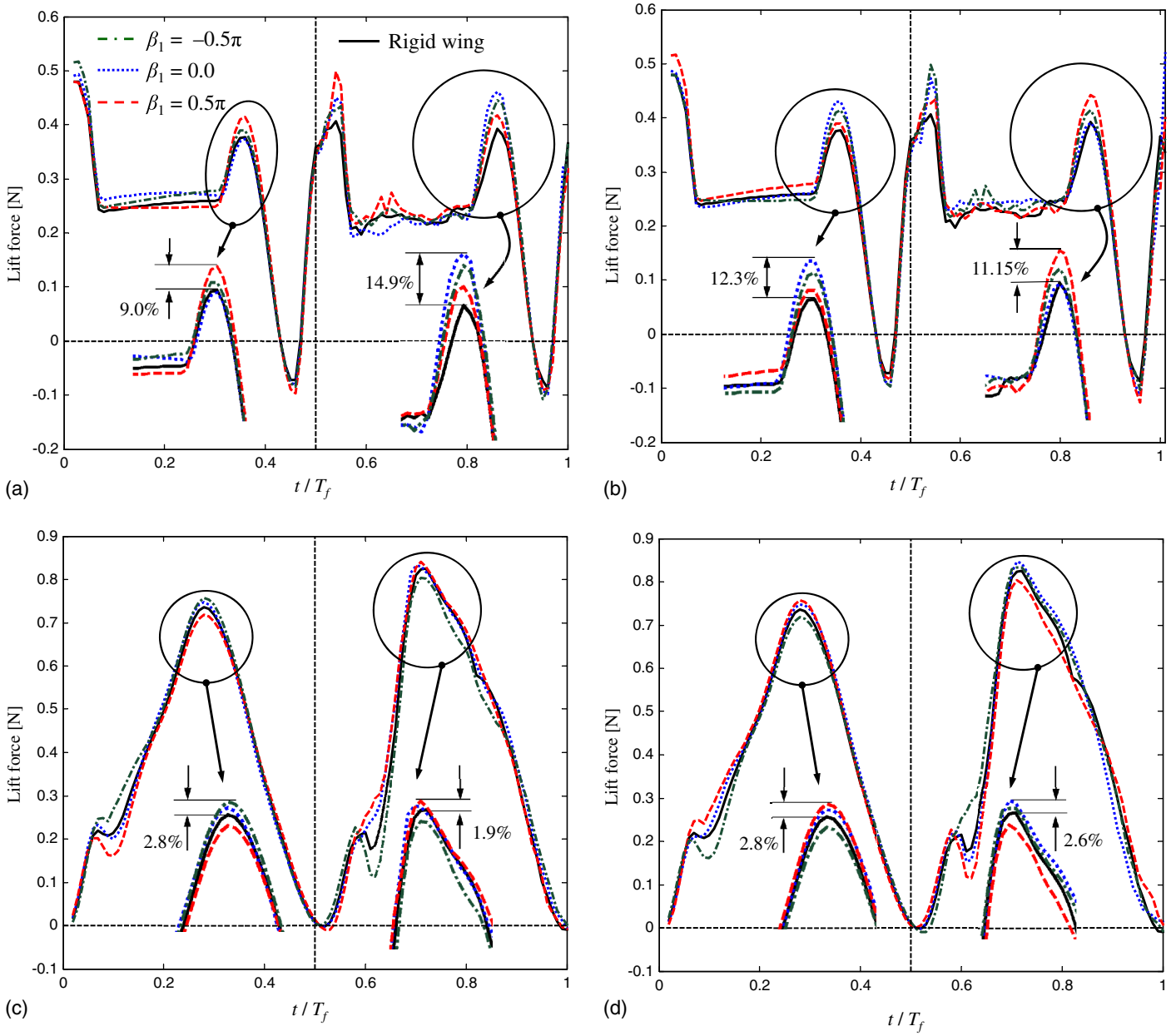

Fig. 11. Influence of IPB on lift: (a) robofly kinematics (IPB1 configuration); (b) robofly kinematics (IPB2 configuration); (c) real kinematics (IPB1 configuration); (d) real kinematics (IPB2 configuration)

Downloaded from ascelibrary.org by Bruno Antonio Roccia on 08/05/16. Copyright ASCE. For personal use only; all rights reserved.

current configuration has a more significant incidence [Figs. 11 (c and d)]. Fig. 12 presents a series of results related to the behavior of the mean lift as a function of the phase angle for both the OPB and the IPB configurations.

From Fig. 12, it is clear that out-of-plane bending has a much stronger influence on the mean value of lift than in-plane bending. The maximum difference between the wing with OPB and the rigid wing for the mean value of lift is 11.2% for the robofly kinematics and 8.8% for the real kinematics. As in the case of twist, results presented in this subsection suggest that in-plane bending can be used in MAVs for increasing lift at specific stages of the stroke cycle.

Combined Deformation Patterns (Twisting + OPB + IPB)

In this subsection, the results of a numerical experiment to quantify the influence of a combination of different deformation types on lift are presented. Particularly, three cases were carefully selected on the basis of the results previously obtained for each deformation pattern in order to maximize lift over the entire stroke cycle.

The analyzed cases differ from each other only in the in-plane bending configuration; the patterns of twist and out-of-plane bending are the same for the three cases (Table 3). In Case 3, IPB is zero throughout the entire flapping cycle. Fig. 13 gives the lifts as functions of time for each configuration in Table 3.

The three cases analyzed in this subsection show a significant increase in lift along a large portion of the stroke cycle. A more precise quantification of this increase produced by each case in Table 3 is obtained by comparing the mean value of the lift against the rigid-wing model as shown in Table 4.

The numerical results presented in this section are a first attempt to qualitatively and quantitatively describe the influence of wing deformations on the lift of flapping wings. Two main deformation mechanism groups can be identified according to the effect they have on lift. The first group is global in nature—that is, increases or decreases in lift occur throughout the entire stroke cycle; such behavior is characteristic of out-of-plane bending. In contrast, the second group can produce the same effects in some, but not all, areas of the stroke cycle or even opposite effects in different areas

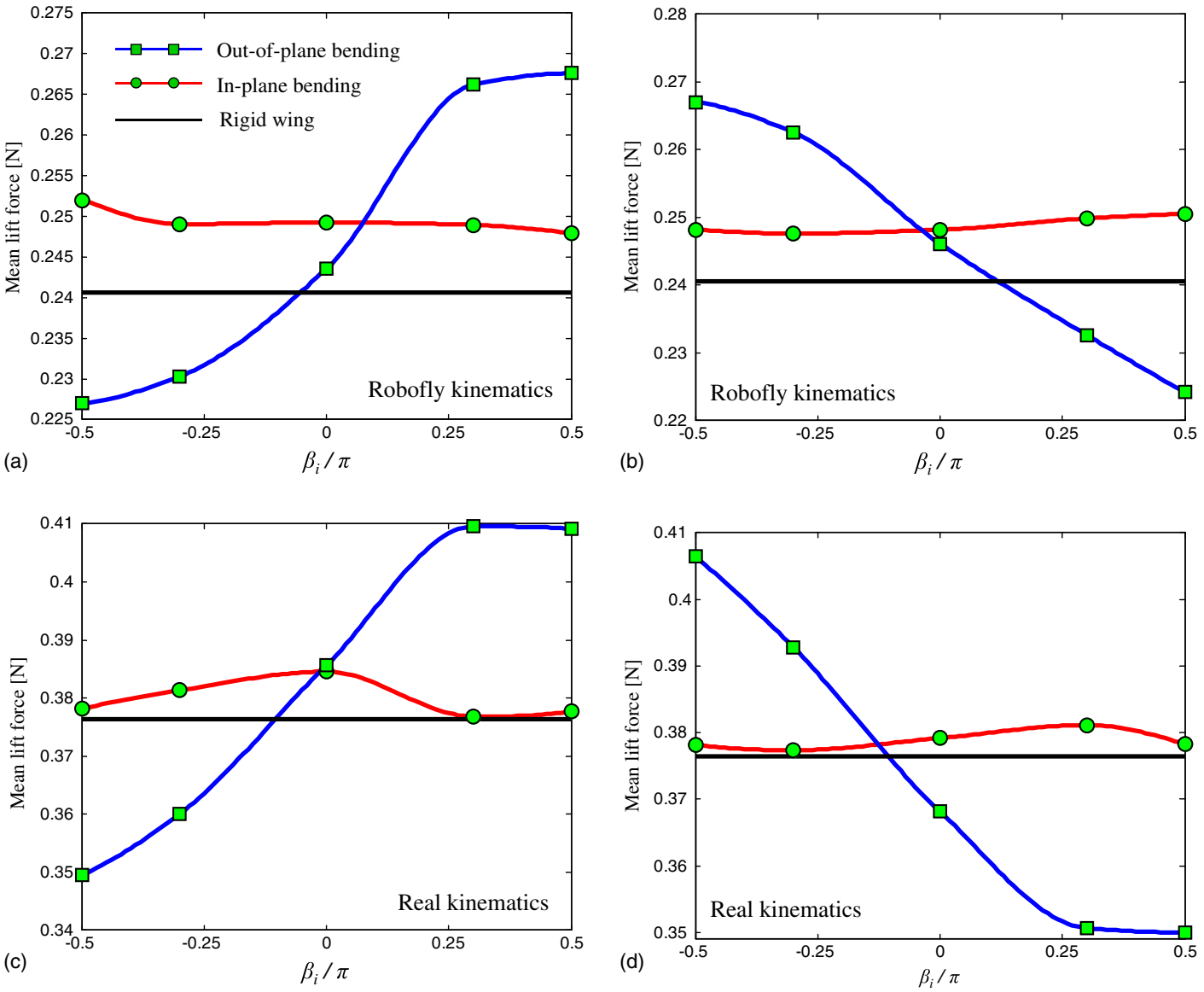

Fig. 12. Mean lift versus phase angle β_i: (a) OPB1 and IPB1 configurations for the robofly kinematics; (b) OPB2 and IPB2 configurations for the robofly kinematics; (c) OPB1 and IPB1 configurations for the real kinematics; (d) OPB2 and IPB2 configurations for the real kinematics

Downloaded from ascelibrary.org by Bruno Antonio Roccia on 08/05/16. Copyright ASCE. For personal use only; all rights reserved.

Table 3. Configurations of the Cases Studied

Case	Twisting	Out-of-plane bending	In-plane bending	Kinematics
1	Advanced pattern	Advanced OPB1 pattern	Advanced IPB1 pattern	Robofly and real
2	Advanced pattern	Advanced OPB1 pattern	Delayed IPB1 pattern	Robofly and real
3	Advanced pattern	Advanced OPB1 pattern	Null	Robofly and real

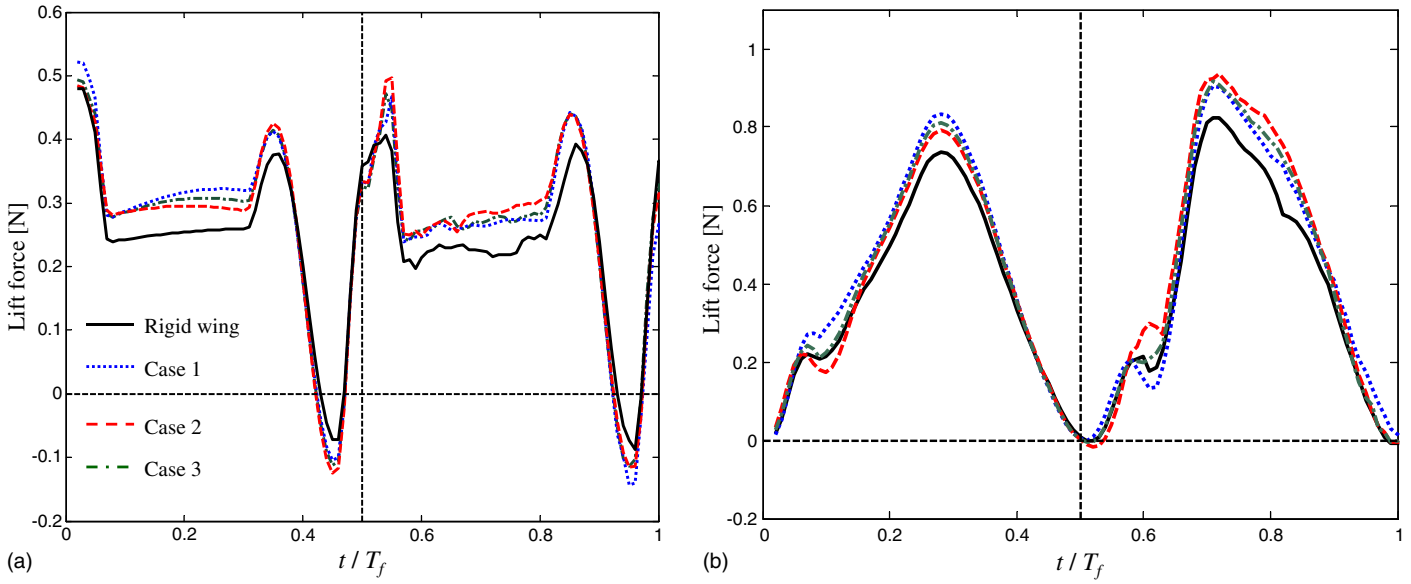

Fig. 13. Influence of the combination of different deformation patterns on lift: (a) robofly kinematics; (b) real kinematics

Table 4. Comparison of Mean Lift—Combined Deformation Patterns

Kinematics	Case	Mean lift (N)
Robofly	Rigid wing	0.24056
	1	0.26389 (+9.70%)
	2	0.26490 (+10.10%)
	3	0.26455 (+10.00%)
Real	Rigid wing	0.37642
	1	0.42106 (+11.80%)
	2	0.42000 (+11.60%)
	3	0.41584 (+10.50%)

of the stroke cycle; such behavior is characteristic of twist and in-plane bending and generally manifests itself as an increase in lift in the rotational phases (pronation/supination) and a decrease in the translational phases (downstroke/upstroke) or vice versa (Figs. 7 and 11).

An important aspect is the way in which different deformation patterns can be combined to produce a specific effect on the aerodynamic performance of a MAV. In this subsection, the main goal is to maximize lift throughout the entire stroke cycle. However, a number of different effects can be achieved by combining deformation mechanisms in different ways. For instance, one can design a deformation pattern that keeps lift constant during the translational phases and maximizes it in the rotational phases, or uses a specific deformation mechanism for the left wing and a different one for the right wing (asymmetric flight) in order to perform some kind of maneuver.

It is noteworthy that all flow fields associated with the cases discussed in this work have very slight differences to discern their relation to the force generation; because of this and in order to keep the article as short as possible, only the flow field of the wing-deformation pattern analyzed in this section is presented. Fig. 14(a) shows how the fluid particles are driven downward as they are shed from the sharp edges, thereby revealing the presence of lift (robofly kinematics). In addition, it can be seen that the aerodynamic model used in this work captures in great detail the simultaneous aerodynamic interference among the wings and wakes and between the two wakes.

In order to expose how the wings deform through the stroke cycle, the shape forms of the wings at several time steps are shown in Fig. 14(b). The deformation of the wings was amplified four times to properly visualize the change in geometry of such lifting surfaces.

Finally, a comprehensive study of wing flexibility on aerodynamic force generation in flapping wings should include phenomena such as wing area expansion and contraction, wing chord bending, and modification and reversal of camber between upstroke and downstroke, among others (Shyy et al. 1999). Another aspect to consider is the development of geometrical nonlinear kinematic models in order to remove limitations such as small displacements/rotations originating in elastic deformations.

Discussion and Future Improvements to Overcome the Limitations of the Model

Although the numerical results obtained using the present model match experimental observations and predict good results for an insect in hover (Roccia et al. 2013), it still is an inviscid model and therefore, has some limitations.

In the computation of the velocity field from the Biot-Savart law, a control point sometimes happens to be very close to a vortex segment. The result is an unreasonably high predicted velocity and therefore an excessive displacement of the aerodynamic nodes (connectors) defining each vortex segment in the wake. These

Downloaded from ascelibrary.org by Bruno Antonio Roccia on 08/05/16. Copyright ASCE. For personal use only; all rights reserved.

Downloaded from ascelibrary.org by Bruno Antonio Roccia on 08/05/16. Copyright ASCE. For personal use only; all rights reserved.

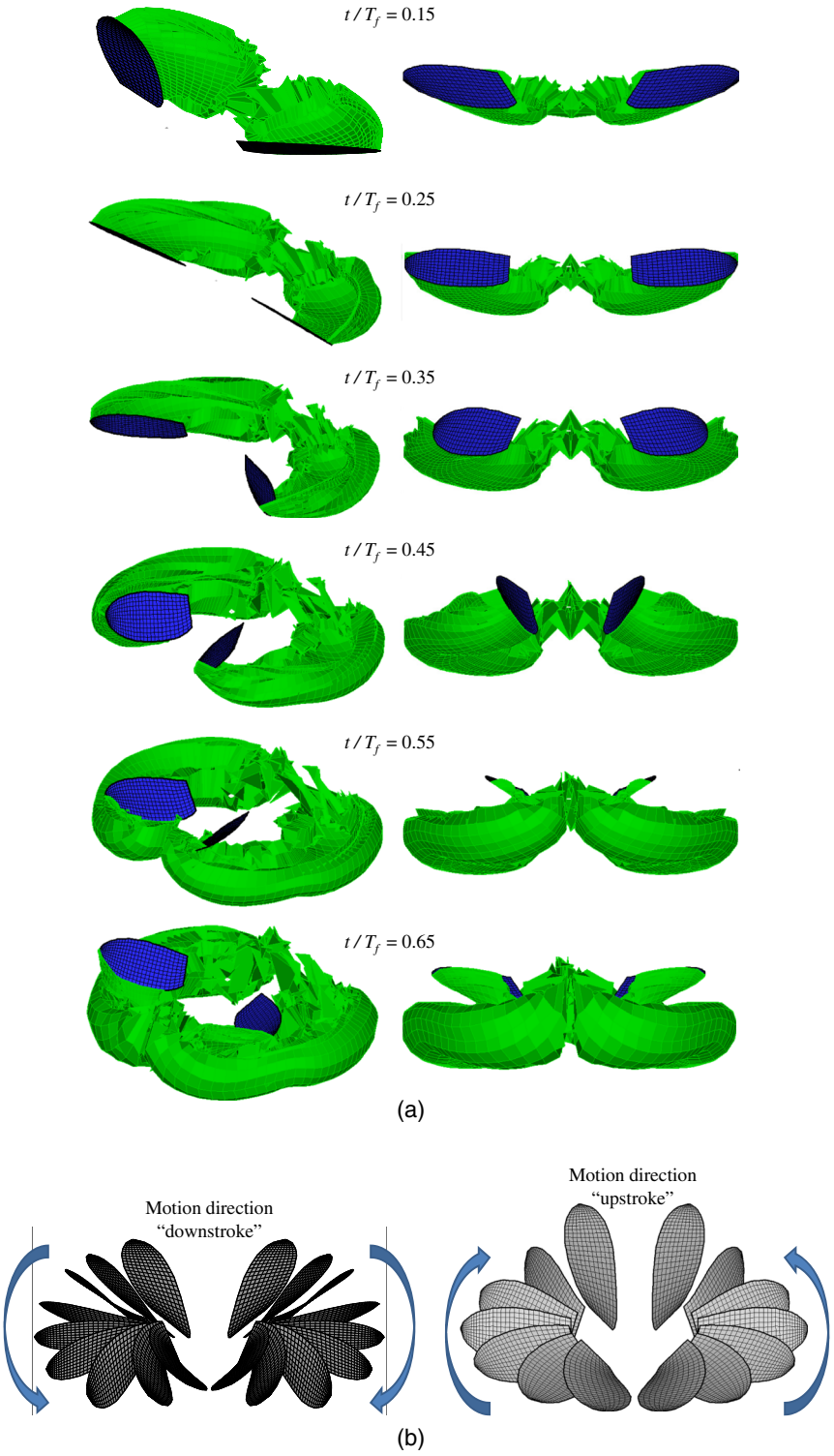

Fig. 14. Numerical simulations for Case I: (a) pattern wake for the first half-stroke; (b) wing deformation through the first stroke cycle (amplified by a factor of four)

numerical instabilities are much more significant in flight configurations in which the wakes remain close around the wings, hovering being an extreme condition (in which the free-stream velocity is zero). Another significant limitation is related to the common situation when a hovering wing cuts through its own wake. Such limitations produce a messy wake from the second translation phase onward, which is directly reflected as a disturbing noise during the second half stroke of all force time-history showed in this work.

The current aerodynamic model needs to be extended to describe wakes as collections of vortex particles, which will improve the numerical treatment and smoothness of wakes (Willis et al. 2007; Koumoutsakos 2005; Winckelmans and Leonard 1993; Cantaloube and Huberson 1984) and, therefore, the resolution of aerodynamic loads. The use of the fast-multipole method to rapidly compute the velocity contribution from the time-varying wakes is also very desirable (Willis et al. 2007; Greengard and Rohklin 1997).

Another limitation is related to the kinematic model, which uses a virtual beam element based on the Euler-Bernoulli model. Because of the importance of wing flexibility to the generation of lift, the current model needs to be extended to investigate the effect of larger deformations on the aerodynamic performance of flapping-wing vehicles.

Despite the limitations outlined in the preceding paragraphs, the modified model presented in this article is an excellent tool for studying the aerodynamics of flying insects, small birds, and flapping-wing MAVs inspired by biology.

Conclusions and Future Work

In this paper, the authors presented a computational framework intended to study the influence of wing flexibility on lift generation in flying insects, small birds, and flapping-wing MAVs.

The aerodynamic model was successfully validated by comparing some present results with the numerical and experimental results of other researchers; the current model is indeed capable of predicting, with notable accuracy, the forces and the flow field generated by insects and MAV-like flapping wings.

Some important conclusions can be drawn from the results presented in the preceding sections. The use of harmonic functions to describe the temporal evolution of in-plane and out-of-plane bending has produced interesting effects on lift. Although this model does not accurately represent the deformation patterns observed in natural flyers, it can be used as a possible mechanism for regulating the aerodynamic forces in MAV-like flapping wings. From the cases considered in this work, the following conclusions can be established:

- Twisting and in-plane bending have a local effect on the lift; they can produce a variety of effects during the stroke cycle, from some changes in specific areas to antagonistic effects between different zones of the flapping cycle, and such influence mainly depends on the timing between the stroke position angle and the generalized coordinate that regulates the deformation pattern;
- Out-of-plane bending, on the contrary, has a global effect on aerodynamic forces; this deformation produces a stronger influence on mean lift than that mentioned previously, either by raising or decreasing it; it was also found that out-of-plane bending strongly depends on the timing between the stroke position angle and the generalized coordinate governing the time variation of this deformation pattern; and
- Through an appropriate combination of the mechanisms of deformation, it is possible to achieve excellent aerodynamic performance; it was shown that a combination of deformation patterns, such as those studied in this work, can lead to a clear increase in lift.

The numerical results presented in this work definitely suggest the strong likelihood that the UVLM can be a very accurate and efficient tool to address further investigations. Currently, a numerical algorithm is being developed to combine the aerodynamic model presented in this work with a dynamical model based on a multibody approach that is also being developed by the authors.

Acknowledgments

This work was partly supported by the Consejo Nacional de Investigaciones Científicas y Técnicas, Argentina. The authors would like to thank the Grupo de Electrónica Aplicada (GEA), Engineering School, Universidad Nacional de Río Cuarto, Argentina and the Grupo de Matemática Aplicada (GMA), Engineering School, Universidad Nacional de Río Cuarto, Argentina.

References

Aguayo, D. D., Santoyo, F. M., De la Torre-I, M. H., Salas-Araiza, M. D., Caloca-Mendez, C., and Gutierrez Hernandez, D. A. (2010). "Insect wing deformation measurements using high speed digital holographic interferometry." *Opt. Express*, 18(6), 5661–5667.

Ansari, S. A., Żbikowski, R., and Knowles, K. (2006a). "Non-linear unsteady aerodynamic model for insect-like flapping wings in the hover. Part 1: Methodology and analysis." *J. Aerosp. Eng.*, 220(2), 61–83.

Ansari, S. A., Żbikowski, R., and Knowles, K. (2006b). "Non-linear unsteady aerodynamic model for insect-like flapping wings in the hover. Part 2: Implementation and validation." *J. Aerosp. Eng.*, 220(3), 169–186.

Baruh, H. (1999). *Analytical dynamics*, McGraw Hill, New York, 107.

Bos, F. M., Lentink, D., van Oudheusden, B. W., and Bijl, H. (2007). "Numerical study of kinematic wing models of hovering insect flight." *45th AIAA Aerospace Sciences Meeting and Exhibit*, AIAA, Reno, NV.

Cantaloube, B., and Huberson, S. (1984). "Calcul d'écoulements de fuide incompressible non visqueux autour de voilures tournantes par une method particulaire." *La Recherche Aérospatiale*, 6, 403–415.

Dalton, S. (1975). *Borne on the wind*, Chatto and Windus, London, 160.

Dalton, S. (1982). *Caught in motion*, Weidenfeld and Nicholson, London, 160.

Dickinson, M. H., Lehmann, F. O., and Sane, S. P. (1999). "Wing rotation and the aerodynamic basis of insect flight." *Science*, 284(5422), 1954–1960.

Du, G., and Sun, M. (2008). "Effects of unsteady deformation of flapping wing on its aerodynamic forces." *Appl. Math. Mech.*, 29(6), 731–743.

Du, G., and Sun, M. (2010). "Effects of wing deformation on aerodynamic forces in hovering hoverflies." *J. Exp. Biol.*, 213(13), 2273–2283.

Ellington, C. P. (1984). "The aerodynamics of hovering insects flight. Part 3: Kinematics." *Phil. Trans. Roy. Soc. Lond. B Biol. Sci.*, 305(1122), 41–78.

Ellington, C. P., Van Den Berg, C., Willmott, A. P., and Thomas, A. L. R. (1996). "Leading-edge vortices in insect flight." *Nature*, 384(6610), 626–630.

Ennos, A. R. (1989). "The kinematics and aerodynamics of the free flight of some Diptera." *J. Exp. Biol.*, 142(1), 49–85.

Fritz, T. E., and Long, L. N. (2004). "Object-oriented unsteady vortex lattice method for flapping flight." *J. Aircraft*, 41(6), 1275–1290.

Ghommem, M., et al. (2012). "Global optimization of actively morphing flapping wings." *J. Fluids Struct.*, 33, 210–228.

Greengard, L., and Rohklin, V. (1997). "A fast algorithm for particle simulations." *J. Comput. Phys.*, 135(2), 280–292.

Intel Corporation. (2003). "Intel Fortran Programmer's Reference." ⟨http://docs.nscl.msu.edu/ifc/intelfor_prglangref.pdf⟩.

Ishilhara, D., Hoire, T., and Denda, M. (2009). "A two-dimensional computational study on the fluid-structure interaction cause of wing pitch changes in dipteran flapping flight." *J. Exp. Biol.*, 212(1), 1–10.

Karnovsky, I. A., and Lebed, O. I. (2000). *Formulas for structural dynamics: Tables, graphs and solutions*, 1st Ed., McGraw Hill, New York, 75.

Konstandinopoulos, P., Mook, D. T., and Nayfeh, A. H. (1981). "A numerical method for general unsteady aerodynamics." *AIAA Atmospheric Flight Mechanics Conf.*, AIAA, Reston, VA, 1981–1877.

Koumoutsakos, P. (2005). "Multiscale flow simulations using particles." *Annu. Rev. Fluid Mech.*, 37, 457–487.

Lehmann, F. O., Gorb, S., Nasir, N., and Schützner, P. (2011). "Elastic deformation and energy loss of flapping fly wings." *J. Exp. Biol.*, 214(17), 2949–2961.

Lentink, D., and Dickinson, M. H. (2009). "Rotational accelerations stabilize leading edge vortices on revolving fly wings." *J. Exp. Biol.*, 212(16), 2705–2719.

Liu, H., Ellington, C. P., Kawachi, K., Van Den Berg, C., and Willmott, A. P. (1998). "A computational fluid dynamic study of hawkmoth hovering." *J. Exp. Biol.*, 201(4), 461–477.

Downloaded from ascelibrary.org by Bruno Antonio Roccia on 08/05/16. Copyright ASCE. For personal use only; all rights reserved.

McMasters, J. H. (1989). "The flight of the bumblebee and related myths of entomological engineering." *Am. Sci.*, 77(2), 164–169.
Mountcastle, A. M., and Combes, S. A. (2013). "Wing flexibility enhances load-lifting capacity in bumblebees." *Proc. Roy. Soc. Ser. B Biol. Sci.*, 280(1759), 1–8.
Murua, J., Palacios, R., and Graham, J. M. R. (2012). "Applications of the unsteady vortex-lattice method in aircraft aeroelasticity and flight dynamics." *Progr. Aerosp. Sci.*, 55, 46–72.
Nakata, T., and Liu, H. (2012). "A fluid-structure interaction model of insect flight with flexible wings." *J. Comput. Phys.*, 231(4), 1822–1847.
Neef, M., and Hummel, D. (2001). "Euler solution for a finite-span flapping wing." *Fixed and flapping wing aerodynamics for micro air vehicle applications*, T. J. Muller, ed., Vol. 195, Progress in Astronautics and Aeronautics, AIAA, Reston, VA, 429–449.
Norberg, R. A. (1972). "The pterostigma of insect wings, an inertial regulator of wing pitch." *J. Comp. Physiol.*, 81(1), 9–22.
Obradovic, B., and Subbarao, K. (2011). "Modeling of flight dynamics of morphing-wing aircraft." *J. Aircraft*, 48(2), 391–402.
Pitt Ford, C. W., and Babinsky, H. (2013). "Lift and the leading-edge vortex." *J. Fluid Mech.*, 720, 280–313.
Preidikman, S. (1998). "Numerical simulations of interactions among aerodynamics, structural dynamics, and control systems." Ph.D. dissertation, Dept. of Engineering Science and Mechanics, Virginia Polytechnic Institute and State Univ., Blacksburg, VA.
Preidikman, S., and Mook, D. T. (2000). "Time-domain simulations of linear and nonlinear aeroelastic behavior." *J. Vib. Control*, 6(8), 1135–1175.
Roccia, B. A., Preidikman, S., Massa, J. C., and Mook, D. T. (2011). "Development of a kinematical model to study the aerodynamics of flapping-wings." *Int. J. Micro Air Vehicles*, 3(2), 61–88.
Roccia, B. A., Preidikman, S., Massa, J. C., and Mook, D. T. (2013). "A modified unsteady vortex-lattice method to study the aerodynamics of flapping wings in hover flight." *AIAA J.*, 51(11), 2628–2642.
Shyy, W., Berg, M., and Ljungqvist, D. (1999). "Flapping and flexible wings for biological and micro air vehicles." *Progr. Aerosp. Sci.*, 35(5), 455–505.
Song, D., Wang, H., Zeng, L., and Yin, C. (2001). "Measuring the camber deformation of a dragonfly wing using projected comb fringe." *Rev. Sci. Instrum.*, 72(5), 2450–2454.
Stanford, B. K., and Beran, P. S. (2010). "Analytical sensitivity analysis of an unsteady vortex-lattice method for flapping-wing optimization." *J. Aircraft*, 47(2), 647–662.
Sun, M., and Tang, J. (2002). "Unsteady aerodynamic force generation by a model fruit fly wing in flapping motion." *J. Exp. Biol.*, 205(1), 55–70.
Taha, H. E., Hajj, M. R., and Nayfeh, A. H. (2012). "Flight dynamics and control of flapping-wing MAVs: A review." *J. Nonlinear Dyn.*, 70(2), 907–939.
Tanaka, H., Whitney, J. P., and Wood, R. J. (2011). "Effect of flexural and torsional wing flexibility on lift generation in hoverfly flight." *Integr. Comp. Biol.*, 51(1), 142–150.
Unger, R., Haupt, M. C., Horst, P., and Radespiel, R. (2012). "Fluid-structure analysis of a flexible flapping airfoil at low Reynolds number flow." *J. Fluid Struct.*, 28, 72–88.
Vanella, M., Fitzgerald, T., Preidikman, S., Balaras, E., and Balachandran, B. (2009). "Influence of flexibility on the aerodynamic performance of a hovering wing." *J. Exp. Biol.*, 212(1), 95–105.
Van Garrel, A. (2003). "The development of a wind turbine aerodynamics simulation module." *ECN Rep. ECN-C-03-079*, Delft Univ. of Technology, Delft, Netherlands.
Walker, S. M., Thomas, A. L. R., Taylor, G. K. (2009a). "Deformable wing kinematics in free-flying hoverflies." *J. Roy. Soc. Lond.*, 7(42), 131–142.
Walker, S. M., Thomas, A. L. R., and Taylor, G. K. (2009b). "Deformable wing kinematics in the desert locust: How and why do camber, twist and topography vary through the stroke?" *J. Roy. Soc. Lond.*, 6(38), 735–747.
Walker, S. M., Thomas, A. L. R., and Taylor, G. K. (2009c). "Photogrammetric reconstruction of high-resolution surface topographies and deformable wing kinematics of tethered locusts and free-flying hoverflies." *J. Roy. Soc. Lond.*, 6(33), 351–366.
Wang, H., Zeng, L., Liu, H., and Yin, C. (2003). "Measuring wing kinematics, flight trajectory and body attitude during forward flight and turning maneuvers in dragonflies." *J. Exp. Biol.*, 206(4), 745–757.
Wang, Z., Chen, P. C., Liu, D. D., Mook, D. T. (2010). "Nonlinear-aerodynamics/nonlinear structure interaction methodology for a high-altitude long-endurance wing." *J. Aircraft*, 47(2), 556–566.
Wang, Z. J., Birch, J. M., and Dickinson, M. H. (2004). "Unsteady forces and flows in flow Reynolds number hovering flight: Two-dimensional computational vs. robotic wing experiments." *J. Exp. Biol.*, 207(3), 449–460.
Weis-Fogh, T. (1973). "Quick estimates of flight fitness in hovering animals, including novel mechanisms for lift production." *J. Exp. Biol.*, 59(1), 169–230.
Wie, S. Y., Lee, S., and Lee, D. J. (2009). "Potential panel and time-marching free-wake coupling analysis for helicopter rotor." *J. Aircraft*, 1041–1030 ,(3)46.
Willis, D. J., Peraire, J., and White, J. K. (2007). "A Combined pFFT-Multipole tree code, unsteady panel method with vortex particle wakes." *Int. J. Numer. Meth. Fluids*, 53(8), 1399–1422.
Winckelmans, G. S., and Leonard, A. (1993). "Contributions to vortex particle methods for the computation of three-dimensional incompressible unsteady flows." *J. Comput. Phys.*, 109(2), 247–273.
Young, J, Walker, S. M., Bomphrey, R. J., Taylor, G. K., and Thomas, A. L. R. (2009). "Details of insect wing design and deformation enhance aerodynamic function and flight efficiency." *Science*, 325(5947), 1549–1552.
Zeng, L., Matsumoto, H., and Kawachi, K. (1996). "A fringe shadow method for measuring flapping angle and torsional angle of a dragonfly wing." *Meas. Sci. Technol.*, 7(5), 786–791.
Zhao, L., Huang, Q. F., Deng, X. Y., and Sane, S. P. (2010). "Aerodynamic effects of flexibility in flapping wings." *J. Roy. Soc. Lond. Interface*, 7 (44), 485–497.
Zheng, L., Hedrick, T. L., and Mittal, R. (2013). "Time-varying wing-twist improves aerodynamic efficiency of forward flight in butterflies." *PLoS One*, 8(1), e53060.

Downloaded from ascelibrary.org by Bruno Antonio Roccia on 08/05/16. Copyright ASCE. For personal use only; all rights reserved.